I&EC research
Industrial & Engineering Chemistry Research
pubs.acs.org/IECR
Article

Stable and Dendrite-Free Zn Anode Enabled by a PEDOT:PSS Layer for High-Performance Zn-Ion Capacitors

Cuiqin Chao, Mengqi Man, Xingchao Wang,* Yan Wu, Fei Zhang, Miaomiao Wu, Qian Xiang, Zhiqiang Luo,* and Ying Sun*

Cite This: *Ind. Eng. Chem. Res.* 2023, 62, 1350−1357
Read Online
ACCESS | Metrics & More | Article Recommendations | Supporting Information

ABSTRACT: Aqueous zinc-ion capacitors (ZICs) are expected to become a new generation of energy storage systems because of their unique advantages. However, the dendritic problem of the Zn anode is still a bottleneck for their large-scale applications. Herein, we introduce a poly(3,4-ethylenedioxythiophene):poly(styrenesulfonate) (PEDOT:PSS) layer on a Zn anode to tackle the dendrite issue. Benefiting from good adhesion and film-forming characteristics, PEDOT:PSS is evenly coated on a zinc anode surface by a simple coating strategy to form a dense artificial film. The well-ordered PEDOT:PSS layer can effectively regulate the deposition direction of zinc ions and effectively prevent water from the zinc surface, resulting in uniform Zn plating/stripping without dendrite growth. A symmetrical cell assembled with PEDOT:PSS@Zn exhibits dendrite-free Zn plating/stripping behavior with stable cycling over 2670 h at a current density of 0.5 mA cm^{-2} and can also operate correctly at 10 mA cm^{-2} for up to 420 h. In addition, this ultrastable anode is equipped with an AC cathode to enable a stable full capacitor with long cycle stability (10,000 cycles).

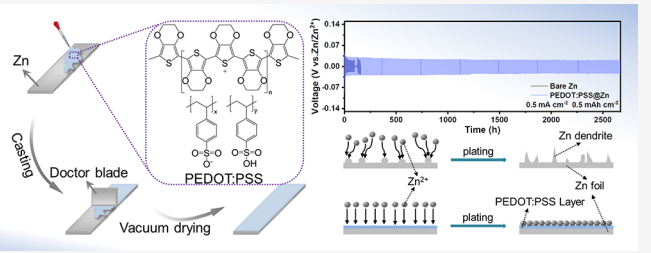

INTRODUCTION

Rechargeable nonaqueous batteries have been a great success in powering new energy vehicles and electric devices, but the inherent high cost, flammability, and volatility of organic electrolytes make nonaqueous batteries unsuitable for large-scale applications. In this regard, rechargeable aqueous batteries (RABs) are receiving increasing attention due to their advantages of low cost, high safety, and high ionic conductivity. Among RABs, aqueous zinc-ion batteries (AZIBs) exhibit great potential for practical applications and can be the primary choice in the future for grid-scale energy storage systems due to their laudable advantages of the properties of Zn anodes, including low Zn plating/stripping potential (−0.76 V vs SHE),[1] high theoretical capacity (820 mAh g^{-1} and 5855 mAh cm^{-3}),[2,3] and excellent stability and reversible Zn plating/stripping in aqueous electrolytes.[4] However, the development of AZIBs is severely hampered by the Zn dendrite problem,[5,6] which poses a significant safety risk to batteries.

Several strategies have been recommended to address the dendrite problem, predominantly focusing on electrolyte engineering and surface modification and the structural construction of Zn anodes. Modulating the electrolyte is considered to be a classic design method to inhibit Zn dendrites. Electrolyte additives (DME,[7] PEO,[8] Mn(CH$_3$COO)$_2$,[9] vanillin,[10] anhydrous acetonitrile,[11] NaClO$_4$,[12] 18-crown-6[13]), highly concentrated electrolytes[14] (25 M ZnCl$_2$ + 5 M NH$_4$Cl,[15] 1 M Zn(OAc)$_2$ + 31 M KOAc,[16] 30 M ZnCl$_2$[17]), and (quasi)-solid electrolytes (PVA,[18] MOF-based,[19,20] gum arabic[21]) can modulate the diffusion behavior of Zn^{2+} ions and thus induce homogeneous Zn plating/stripping. The construction of multidimensional zinc hosts has proved to be a practical method for inducing the homogeneous deposition of Zn^{2+} ions. Surface modification of Zn anodes with organic polymers (polyamides,[22] PVDF,[23] PAN,[24] MXene-mPPy[25]) or inorganic materials (carbon,[26,27] metal oxides,[28−32] alloy,[33] and MXene[34−36]) to construct the protective layer is another simple and effective method. These artificial layers not only avoid direct contact between the Zn anode and the electrolyte, preventing the occurrence of side reactions, but also change the electric field distribution to yield the uniform deposition of Zn^{2+} ions. Unfortunately, conventional artificial layers commonly require the addition of binders and it is difficult to achieve industrial production using complex processes.

In this work, we present a unique binder-free poly(3,4-ethylenedioxythiophene):poly(styrenesulfonate) (PE-

Received: September 24, 2022
Revised: January 2, 2023
Accepted: January 2, 2023
Published: January 12, 2023

https://doi.org/10.1021/acs.iecr.2c03462
Ind. Eng. Chem. Res. 2023, 62, 1350−1357

DOT:PSS) film for a dendrite-free zinc anode. PEDOT:PSS, a commercially conductive polymer with good stretchability, high conductivity, and facile film-forming ability, is widely used for wearable, flexible, and stretchable devices. The PEDOT:PSS artificial protective layer can not only inhibit corrosion reactions and byproducts but also inhibit Zn dendrites by controlling the nucleation and growth of Zn, which is preferentially deposited on the (002) crystal plane. As a result, the symmetrical cell assembled with PEDOT:PSS@Zn can be stably cycled for more than 2670 h at a current density of 0.5 mA cm^{-2}. Even at a higher current density of 10 mA cm^{-2}, the symmetrical cells show good cyclability for more than 420 h, outperforming that of the Zn//Zn symmetrical cells. Zinc-ion capacitors (ZICs) assembled with this anode and the activated carbon (AC) cathode exhibited excellent long cycling performance by being stable for 10,000 cycles.

EXPERIMENTAL SECTION

Materials. Zinc sulfate ($ZnSO_4$, 99.995%) was purchased from Aladdin. Zn foils (0.1 mm in thickness) and Ti foils (0.03 mm in thickness) were bought from Shengshida Metal Materials Co. Ltd. Poly(3,4-ethylenedioxythiophene)-poly-(styrenesulfonate) 1.1 wt % in H_2O (PEDOT:PSS) was purchased from Sigma-Aldrich. Active carbon (AC, YP-80F) was obtained from Kuraray.

Preparation of the Integrated PEDOT:PSS@Zn Electrodes. First, a mixture of PEDOT:PSS aqueous solution and anhydrous ethanol (1:1 by volume) was applied to the surface of the zinc foil by scraping and then being dried in a vacuum oven at 80 °C. Next, the dried zinc foil was cut into circular pieces with a diameter of 12 mm to obtain the integrated PEDOT:PSS@Zn electrodes. The PEDOT:PSS@Ti electrode was produced by replacing the zinc foil with a titanium foil using the method described above.

Preparation of AC Cathodes. First, 70 wt % AC powder, 20 wt % KB, and 10 wt % PVDF were mixed with *N*-methyl-2-pyrrolidone (NMP) to form a slurry. Then, the slurry was applied to the Ti foil and dried in a vacuum oven at 60 °C to obtain the AC cathode.

Characterization. The contact angles of the bare Zn electrode and the integrated PEDOT:PSS@Zn electrode were measured by an optical contact angle goniometer (DSA25S, Kruss, Germany). At room temperature, the contact angle was tested by applying 2 M $ZnSO_4$ electrolyte with 10 μL on the surface of the electrode sheet.

The surface morphology of the samples was viewed by a field emission scanning electron microscope (SEM, S-4800, Hitachi, Japan). Changes in the functional groups of the samples were characterized by a Fourier infrared spectrometer (FTIR, VERTEX70, Bruker, Germany). Chemical bonding changes on the surface of the samples were analyzed by an X-ray photoelectron spectrometer (XPS, ESCALAB 250Xi, Thermo Fisher Scientific). X-ray diffraction (XRD, Smart Lab SE, Rigaku, Japan) was used to explore the evolution of crystal structures.

Electrochemical Measurements. CR2016-type aqueous zinc-ion coin batteries were assembled using a glass fiber (GF/F) as a separator and 2 M $ZnSO_4$ as the electrolyte. For testing the Coulombic efficiency (CE), charge and discharge tests were carried out in a LAND test system (Wuhan Land, China) using bare Zn as the anode and Ti foil or PEDOT:PSS@Ti as the cathode. For the full cell, a CR2016 coin cell was assembled using a bare Zn electrode or the integrated PEDOT:PSS@Zn electrode as the anode and activated carbon as the cathode. The CHI760E (Chenhua, China) electrochemical workstation was used to measure cyclic voltammetry (CV) and linear polarization. The CVs of the Zn//Ti and Zn//PEDOT:PSS@Ti half-cells were observed at the operational voltage range of −0.2−1.2 V and the scan rate of 1 mV s^{-1}. Linear polarization curves were obtained using Zn or PEDOT:PSS@Zn symmetrical cells at the scan rate of 2 mV s^{-1}. The assembled Zn or PEDOT:PSS@Zn symmetrical cells were performed by a VMP-300 multichannel electrochemical workstation (Bio-Logic, France) for chronoamperograms (CAs).

RESULTS AND DISCUSSION

PEDOT:PSS is a kind of high molecular polymer with wonderful film-forming property and can be coated directly onto the surface of the zinc foil to gain the integrated PEDOT:PSS@Zn electrode (Scheme 1). Figure 1a,b displays the SEM images and optical pictures of the bare Zn electrode and the integrated PEDOT:PSS@Zn electrode. Commercially available silvery white zinc foil with a rich metallic sheen has a rough, uneven surface (inset of Figure 1a). The integrated PEDOT:PSS@Zn electrode with a protective layer thickness of approximately 6 μm (Figure S1) shows a blue surface (inset of Figure 1b). The atomic force microscopy (AFM) images (Figure S2) more visually present that the integrated PEDOT:PSS@Zn electrode has a smooth and flat surface, which facilitates the uniform distribution of the electric field on

Scheme 1. Schematic Illustration of the Construction of the PEDOT:PSS@Zn Electrode

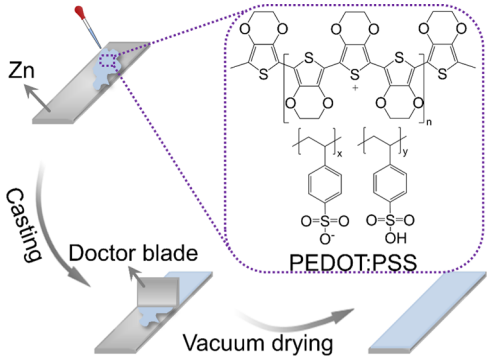

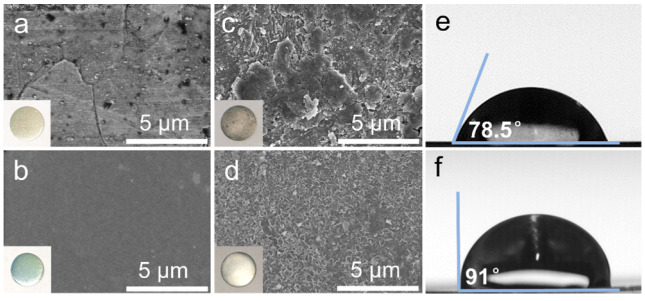

Figure 1. SEM images of the (a) bare Zn electrode, (b) integrated PEDOT:PSS@Zn electrode, (c) soaked bare Zn electrode, and (d) soaked integrated PEDOT:PSS@Zn electrode. Contact angles of the 2 M $ZnSO_4$ electrolyte on the surface of the (e) bare Zn electrode and (f) integrated PEDOT:PSS@Zn electrode, respectively.

https://doi.org/10.1021/acs.iecr.2c03462
Ind. Eng. Chem. Res. 2023, 62, 1350−1357

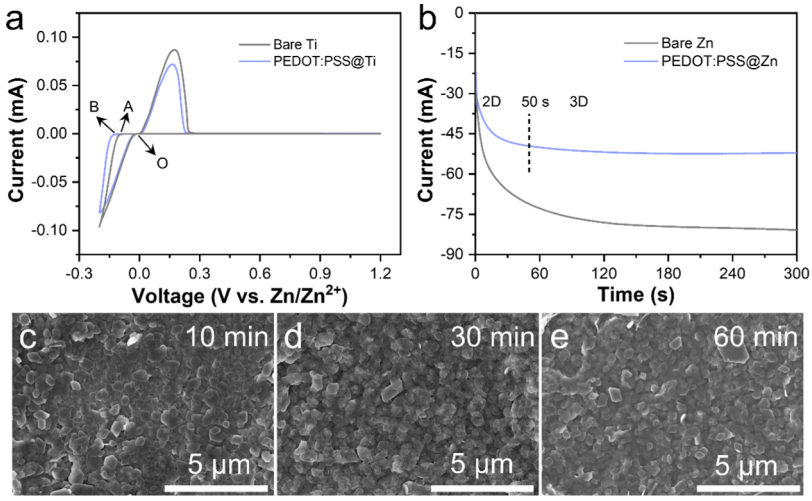

Figure 2. (a) Cyclic voltammograms for Zn nucleation on the bare Ti foil and PEDOT:PSS@Ti electrodes. (b) Chronoamperograms of the bare Zn electrode and the integrated PEDOT:PSS@Zn electrode at the overpotential of −150 mV. (c−e) SEM images of the integrated PEDOT:PSS@Zn electrode after deposition at a current density of 1 mA cm^{-2} over different times.

the electrode surface, inhibits the selective deposition of Zn^{2+}, and promotes the uniform nucleation and growth of Zn^{2+}.

Figure S3a shows the Raman spectra of the integrated PEDOT:PSS@Zn electrode. The polymer PSS has a dominant weight in PEDOT:PSS, but the Raman scattering cross section of PSS is very weak. In contrast, the Raman bands are mainly contributed by PEDOT and have been described in detail as follows. The bands at 1552 and 1518 cm^{-1} are attributed to the asymmetric $C_\alpha{=}C_\beta$ stretching mode. The bands at 1432, 1369, and 1270 cm^{-1} correspond to symmetric $C_\alpha{=}C_\beta$, symmetric $C_\beta{=}C_\beta$, and $C_\alpha{=}C_\alpha'$ inter-ring stretching vibrations. A weaker band at 1096 cm^{-1} is assigned to C−O−C deformation, while the peaks at Raman shifts of 991 and 574 cm^{-1} are attributed to oxyethylene ring deformation. The characteristic peak at 441 cm^{-1} is derived from SO_2 bending. In addition, XPS was performed on the integrated PEDOT:PSS@Zn electrode. Figure S3b shows the full spectra of the integrated PEDOT:PSS@Zn electrode, demonstrating the presence of Zn, C, O, and S elements. In the S 2p spectra, the two peaks at 169.4 and 168.1 eV are attributed to the sulfonic acid group of PSS, and the peaks at 164.7 and 163.5 eV are derived from the thiophene group of the PEDOT molecule (Figure S3c).[37] The high-resolution Zn 2p spectra present two strong peaks at 1022.2 and 1045.3 eV for $2p_{3/2}$ and $2p_{1/2}$ of Zn^0, respectively (Figure S3d). The above characterization indicates that PEDOT:PSS is successfully applied to the surface of the Zn foil, but without chemical bonding between the Zn foil and the PEDOT:PSS coating.

To investigate the effect of PEDOT:PSS artificial coatings on inhibiting anodic surface corrosion, contact angle tests, corrosion experiments, and linear polarization tests were carried out. The contact angle test was measured by dropping the 2 M $ZnSO_4$ electrolyte onto the anode surface (Figure 1e,f). The contact angle of the integrated PEDOT:PSS@Zn surface is about 91°, higher than that on the bare Zn surface (78.5°), showing the good hydrophobic properties of the PEDOT:PSS protective layer. This property can avoid direct contact between water molecules and Zn, thus potentially slowing down the corrosion rate. To verify the corrosion-resistant properties of the PEDOT:PSS coating, SEM and XRD analyses were carried out on the bare Zn electrode and the integrated PEDOT:PSS@Zn electrode after 10 days of soaking in a 2 M $ZnSO_4$ electrolyte (Figure S4). The bare Zn surface loses its metallic luster and becomes more uneven after immersion (Figure 1c), displaying severe corrosion. Correspondingly, the integrated PEDOT:PSS@Zn electrode exhibits almost no significant change in surface color (Figure S4c) and a bright surface even after removal of the artificial coating (inset of Figure 1d). The SEM images suggest that the surface morphology of the integrated PEDOT:PSS@Zn electrode after soaking is uniform and flat (Figure 1d). As expected, the XRD characterization (Figure S5) confirms more byproducts on the bare Zn electrode than on the integrated PEDOT:PSS@Zn electrode, indicating that the PEDOT:PSS artificial protective layer effectively inhibits electrolyte corrosion of the electrode. Furthermore, the reduction of corrosion currents in the linear polarization curves further demonstrates that the PEDOT:PSS coating can inhibit the corrosion of the Zn anode (Figure S6).

The effect of the PEDOT:PSS protective layer on the behavior of Zn deposition was further investigated by CV and CA tests. The CVs were performed using coin-type cells with zinc foil as counter electrodes and the PEDOT:PSS@Ti electrode as the working electrode. On the one hand, as shown in Figure 2a, bare Ti and PEDOT:PSS@Ti electrodes show similar CVs, which confirm their similar electrochemical behavior. On the other hand, the nucleation overpotential of the Zn//PEDOT:PSS@Ti cells (point O to point B) is higher than that of the Zn//Ti cells (point O to point A), suggesting that the PEDOT:PSS coating reduces the deposition rate of Zn^{2+} at the integrated PEDOT:PSS@Zn electrodes, which is more favorable to increase the Zn^{2+} sites and inhibit the growth of Zn dendrites. To scrutinize the nucleation behavior, CA tests were performed at a constant overpotential of −150 mV using symmetric cells (Figure 2b). The CA curves measured for the cell with the integrated PEDOT:PSS@Zn electrode tend to stabilize after 50 s. This phenomenon implies Zn^{2+} shifts to smooth three-dimensional diffusion (3D) after a short two-dimensional planar diffusion (2D) process, which contributes to the formation of a flat and dense deposition layer on the anode surface.[38] In contrast, the symmetric cells with a bare Zn electrode present a continuous current growth, indicating a long 2D diffusion of Zn^{2+}, which leads to the

https://doi.org/10.1021/acs.iecr.2c03462
Ind. Eng. Chem. Res. 2023, 62, 1350−1357

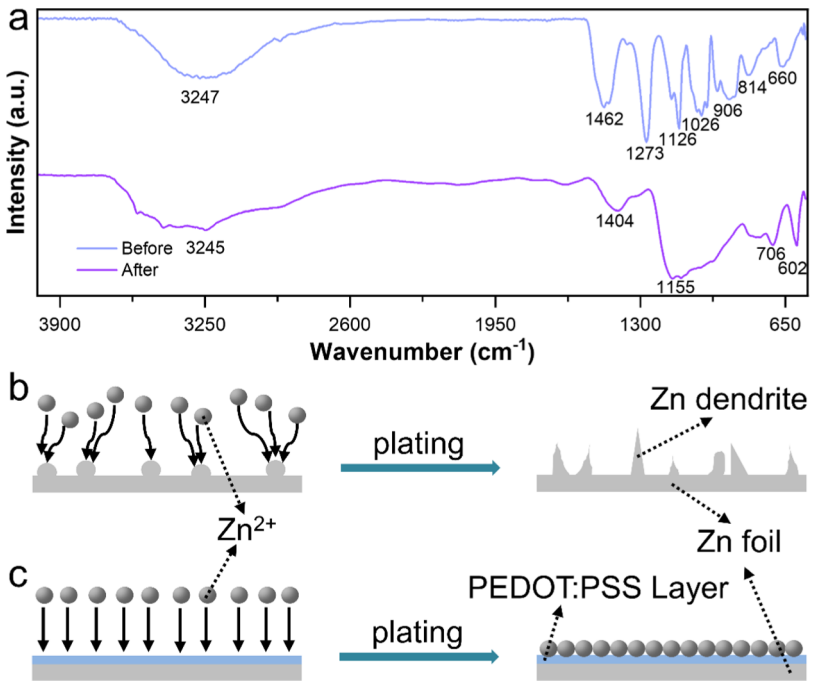

Figure 3. (a) FTIR spectra of the integrated PEDOT:PSS@Zn electrode and after cycling at the current density of 10 mA cm^{-2}. Schematic illustrations of Zn^{2+} plating on the (b) bare Zn electrode and (c) integrated PEDOT:PSS@Zn electrode.

disordered nucleation of Zn^{2+} on the Zn anode surface and the continuous growth at the tip to form Zn dendrites.

SEM was employed to evaluate the effect of the integrated PEDOT:PSS layer on the morphologies of Zn deposition. As shown in Figure 2c, a large number of uniform flakes are formed on the surface of the integrated PEDOT:PSS@Zn electrode after plating for 10 min. The same morphological distribution appears on the surface of the integrated PEDOT:PSS@Zn electrode with the deposition time ranging from 30 (Figure 2d) to 60 min (Figure 2e). In addition, the surface morphologies of the bare Zn electrode and the integrated PEDOT:PSS@Zn electrode after cycling were also characterized by SEM. After cycling at a current density of 1 mA cm^{-2}, the surface of the bare Zn electrode displays selective deposition and irregular pile-up growth (Figure S7a,b), which is caused by the rough and uneven surface of bare Zn, resulting in a nonuniform distribution of the electric field between the electrode and the electrolyte. Fortunately, Zn^{2+} is deposited as regular polygonal flakes on the surface of the integrated PEDOT:PSS@Zn electrode, probably owing to the protective layer providing a flat surface and balancing the electric field distribution, allowing Zn^{2+} to be deposited uniformly in regular directions. Moreover, the role of the PEDOT:PSS layer in inducing Zn^{2+} deposition was further verified at an ultrahigh current density of 10 mA cm^{-2} (Figure S7c,f). In addition, a simple visual cell was designed to visualize the deposition of Zn^{2+} on the surface of the integrated PEDOT:PSS@Zn electrode. The integrated PEDOT:PSS@Zn electrode changes from its original blue color to a silvery white color after 1 h of continuous plating at a current density of 10 mA cm^{-2} (Figure S8), signifying that Zn^{2+} is deposited on the surface of the integrated PEDOT:PSS@Zn electrode. The results demonstrate that the PEDOT:PSS coating can act as an inhibitor of Zn dendrites. The evolution of the crystal structure of the electrode after Zn deposition was analyzed by XRD. Remarkably, the peak intensity of the (002) crystal plane for the integrated PEDOT:PSS@Zn electrode is significantly enhanced than for the bare Zn electrode after plating for 1 h at 2 mA cm^{-2} (Figure S9). This result indicates that the PEDOT:PSS coating promotes the preferential growth of the (002) crystal plane and achieves the inhibition of Zn dendrite growth.

To investigate the inhibiting Zn dendrite mechanism of the PEDOT:PSS coating in more depth, the integrated PEDOT:PSS@Zn before and after cycling was studied by Fourier transform infrared spectroscopy (FTIR) and XPS. In the FTIR spectra of the integrated PEDOT:PSS@Zn electrode (Figure 3a), the peak at 3247 cm^{-1} is derived from the bending deformation vibration absorption peak of the O−H bond of the residual water molecule. In addition, the peaks at 1462 and 1273 cm^{-1} are ascribed to the C═C of the thiophene ring. The absorption peaks at 1126 and 1026 cm^{-1} correspond to the C−O−C bonds of the dioxythiophene ring and the S−O and S-phenyl of the sulfonic acid group. The peaks at 906, 814, and 660 cm^{-1} correspond to the C−S bond of the thiophene ring. However, the FTIR absorption feature peak of the integrated PEDOT:PSS@Zn electrode changes significantly after 40 h at a current density of 10 mA cm^{-2}. The characteristic C−C absorption peak of the thiophene ring at 1273 cm^{-1} disappears, while a new large broad peak at 1155 cm^{-1} appears, which may be attributed to the interaction of PEDOT:PSS and Zn^{2+} during cycling. Meanwhile, the high-resolution S 2p spectra in the XPS spectra (Figure S10) indicate that the PEDOT characteristic spectra of the integrated PEDOT:PSS@Zn electrode disappear after Zn plating/stripping, further explaining that the S-based functional group in the thiophene ring can combine with Zn^{2+} during plating to induce uniform Zn deposition (Figure S10).

The flat surface and S-based functional groups of the PEDOT:PSS coating play a crucial role in the nucleation and growth of Zn^{2+}. The schematic diagram in Figure 3 briefly depicts the deposition process of Zn^{2+} on the surface of the

https://doi.org/10.1021/acs.iecr.2c03462
Ind. Eng. Chem. Res. 2023, 62, 1350−1357

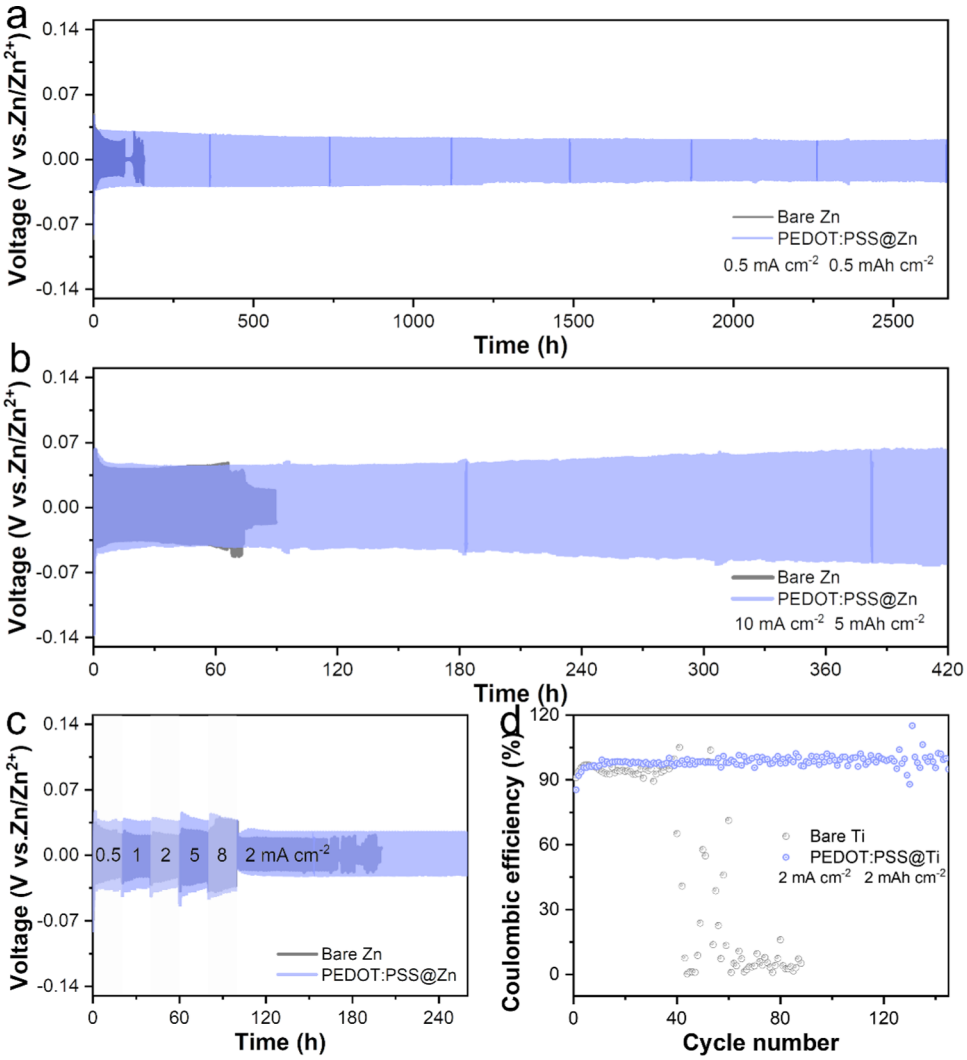

Figure 4. Voltage profiles of the symmetric cells during Zn plating/stripping at different current densities: (a) 0.5 mA cm^{-2} for 0. 5 mAh cm^{-2}, (b) 10 mA cm^{-2} for 5 mAh cm^{-2}, and (c) rate performance at 0.5, 1, 2, 5, and 8 mA cm^{-2} of 1 h. (d) CE of Zn//Ti cells and Zn//PEDPT@Ti cells at 2 mA cm^{-2} for 2 mAh cm^{-2}.

bare Zn electrode and the integrated PEDOT:PSS@Zn electrode. On the one hand, bare Zn in contact with an electrolyte is subject to severe corrosion and side reaction problems. On the other hand, Zn^{2+} selectively nucleates and continuously grows to form dendrites on the bumpy surface of the bare Zn electrode due to its uneven surface during the Zn plating/stripping process (Figure 3b). By contrast, the PEDOT:PSS coating on the surface of the integrated PEDOT:PSS@Zn electrode alleviates corrosion and side reaction problems by avoiding direct contact between the electrolyte and the Zn substrate. In addition, the integrated PEDOT:PSS@Zn electrode surface coating anchors the Zn^{2+} while balancing the electric field distribution near the anode, inducing uniform Zn-ion deposition preferentially in the direction of the $(002)_{Zn}$ crystal plane and inhibiting Zn dendrites (Figure 3c).

The electrochemical stability of the integrated PEDOT:PSS@Zn electrode was estimated by assembling symmetric cells under constant current conditions. As can be seen in Figure 4a, the Zn//Zn symmetrical cells short circuit after only 82 h of cycling at a current density of 0.5 mA cm^{-2} and an area-specific capacity of 0.5 mAh cm^{-2}, probably due to the amount of Zn dendrites produced on the electrode during charging and discharging. Notably, PEDOT:PSS@Zn//PEDOT:PSS@Zn symmetrical cells can be cycled stably for 2670 h (Figure S12c) with the same conditions, showing an excellent cycling life and a stable voltage distribution. Meanwhile, the integrated PEDOT:PSS@Zn electrode can also achieve a stable Zn plating/stripping ability for up to 2950 h at a lower current density of 0.25 mA cm^{-2} (Figure S11). As can be seen from Figure 4b, even at a high current density of 10 mA cm^{-2}, the PEDOT:PSS@Zn//PEDOT:PSS@Zn symmetrical cells achieve stable Zn plating/stripping with no significant voltage fluctuations, which is much better than that of the Zn//Zn symmetrical cells. It is noted that the polarization of the former symmetrical cells (63.9 mV) is slightly higher than that of the latter (60.1 mV) (Figure S12), which may be due to the hydrophobic nature of PEDOT:PSS (Figure 1e,f). Surprisingly, this work extends the lifetime of the Zn anode and offers more commercial advantages than some previous reports on Zn anode coating protection (Table S1). As shown in Figure 4c, the Zn//Zn symmetrical cells short circuit within 163 h after cycling at different current densities, while the PEDOT:PSS@Zn//PEDOT:PSS@Zn symmetrical

https://doi.org/10.1021/acs.iecr.2c03462
Ind. Eng. Chem. Res. 2023, 62, 1350−1357

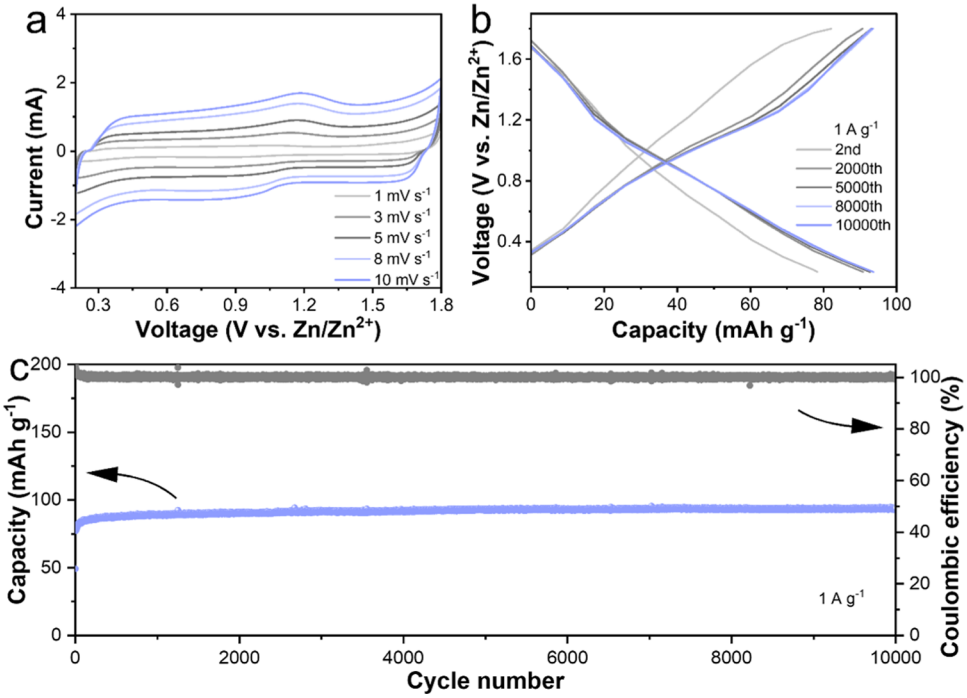

Figure 5. Electrochemical performance of Zn//AC ZICs. (a) CV curves at different scan rates. (b) Galvanostatic charge/discharge curves. (c) Long cycle performance.

cells remain stable for over 250 h of cycling, showing good reversibility and rate performance. Figure 4d shows the CE of Zn//Ti and Zn//PEDOT:PSS@Ti cells tested at a constant current density of 2 mA cm^{-2}. The cell assembled with the PEDOT:PSS@Ti can be cycled 145 cycles consistently, with an average CE of 98.5%, significantly better than that of the bare Ti cell (30 cycles, 94.3%), which strongly confirms that the PEDOT:PSS coating can improve the reversibility of Zn plating/stripping.

A typical PEDOT:PSS@Zn//AC capacitor was assembled to explore the feasibility of the integrated PEDOT:PSS@Zn anode (Figure 5). The energy storage mechanism for this energy storage device is Zn plating/stripping at the Zn anode and physical adsorption/desorption of ions at the AC cathode. The CVs (Figure 5a) of the PEDOT:PSS@Zn//AC cell at different scan rates show similar electrochemical behavior, indicating excellent kinetic performance. Surprisingly, the PEDOT:PSS@Zn//AC capacitor still has a capacity of 93.5 mAh g^{-1} after 10,000 cycles, corresponding to an energy density of 76.4 Wh kg^{-1} and a power density of 816.1 W kg^{-1}, which is superior to that of most reports (Figure 5c and Table S2). Also, the galvanostatic charge−discharge curves for different numbers of cycles (Figure 5b) further confirm that the system is repeatable and extremely stable. The excellent electrochemical performance of the PEDOT:PSS@Zn//AC capacitor better proves the performance of the integrated PEDOT:PSS@Zn anode.

CONCLUSIONS

In summary, we demonstrated a straightforward strategy of using a binder-free conductive polymer PEDOT:PSS protective layer on the surface of the Zn anode to overcome the Zn dendrites and corrosion problems of AZIBs. Thanks to its good electronic conductivity and S-functional groups, the PEDOT:PSS layer can balance electric field distribution and induce uniform nucleation of Zn at the (002) crystal plane, while reducing the two-dimensional diffusion time of Zn^{2+}. As a result, the PEDOT:PSS@Zn//PEDOT:PSS@Zn symmetrical cells can be stably cycled for more than 2670 h at a current density of 0.5 mA cm^{-2}, outperforming that of the Zn//Zn symmetrical cells. In addition, the assembled ZICs with the integrated PEDOT:PSS@Zn anodes and AC cathodes exhibit impressive cyclability with a long life of over 10 000 cycles at 1 A g^{-1}, demonstrating great potential for practical applications. This work demonstrates the importance of the surface coating strategy for Zn anodes to build long-life, stable AZIBs.

ASSOCIATED CONTENT

Supporting Information

The Supporting Information is available free of charge at https://pubs.acs.org/doi/10.1021/acs.iecr.2c03462.

SEM cross section for the PEDOT:PSS@Zn electrode; 3D AFM of bare Zn and PEDOT:PSS@Zn electrodes; Raman and XPS of the PEDOT:PSS@Zn electrode; optical images of the bare Zn electrode and PEDOT:PSS@Zn electrode before and after soaking; XRD patterns of the bare Zn electrode and the PEDOT:PSS@Zn electrode before and after 10 days of soaking; linear polarization curves of the bare Zn electrode and the PEDOT:PSS@Zn electrode; visual PEDOT:PSS@Zn symmetrical cell; high-resolution XPS of PEDOT:PSS@Zn before and after the cycling; and Zn plating/stripping voltage profiles of the PEDOT:PSS@Zn symmetrical cell (PDF)

AUTHOR INFORMATION

Corresponding Authors

Xingchao Wang − *State Key Laboratory of Chemistry and Utilization of Carbon Based Energy Resources, Key*

https://doi.org/10.1021/acs.iecr.2c03462
Ind. Eng. Chem. Res. 2023, 62, 1350−1357

Laboratory of Advanced Functional Materials, Autonomous Region, Institute of Applied Chemistry, College of Chemistry, Xinjiang University, Urumqi 830046 Xinjiang, P. R. China; orcid.org/0000-0001-7380-9618; Email: ichemabc@126.com

Zhiqiang Luo − *Tianjin Key Lab for Photoelectric Materials & Devices, School of Materials Science and Engineering, Tianjin University of Technology, Tianjin 300384, P. R. China;* orcid.org/0000-0002-1332-1335; Email: zhqluo@email.tjut.edu.cn

Ying Sun − *Key Laboratory of Improvised Explosive Chemicals for State Market Regulation, Xinjiang Uygur Autonomous Region Product Quality Supervision and Inspection Institute, Urumqi 830011 Xinjiang, P. R. China*; Email: emma9955@126.com

Authors

Cuiqin Chao − *State Key Laboratory of Chemistry and Utilization of Carbon Based Energy Resources, Key Laboratory of Advanced Functional Materials, Autonomous Region, Institute of Applied Chemistry, College of Chemistry, Xinjiang University, Urumqi 830046 Xinjiang, P. R. China*

Mengqi Man − *State Key Laboratory of Chemistry and Utilization of Carbon Based Energy Resources, Key Laboratory of Advanced Functional Materials, Autonomous Region, Institute of Applied Chemistry, College of Chemistry, Xinjiang University, Urumqi 830046 Xinjiang, P. R. China*

Yan Wu − *State Key Laboratory of Chemistry and Utilization of Carbon Based Energy Resources, Key Laboratory of Advanced Functional Materials, Autonomous Region, Institute of Applied Chemistry, College of Chemistry, Xinjiang University, Urumqi 830046 Xinjiang, P. R. China*

Fei Zhang − *State Key Laboratory of Chemistry and Utilization of Carbon Based Energy Resources, Key Laboratory of Advanced Functional Materials, Autonomous Region, Institute of Applied Chemistry, College of Chemistry, Xinjiang University, Urumqi 830046 Xinjiang, P. R. China*

Miaomiao Wu − *State Key Laboratory of Chemistry and Utilization of Carbon Based Energy Resources, Key Laboratory of Advanced Functional Materials, Autonomous Region, Institute of Applied Chemistry, College of Chemistry, Xinjiang University, Urumqi 830046 Xinjiang, P. R. China*

Qian Xiang − *State Key Laboratory of Chemistry and Utilization of Carbon Based Energy Resources, Key Laboratory of Advanced Functional Materials, Autonomous Region, Institute of Applied Chemistry, College of Chemistry, Xinjiang University, Urumqi 830046 Xinjiang, P. R. China*

Complete contact information is available at: https://pubs.acs.org/10.1021/acs.iecr.2c03462

Author Contributions

C.C.: methodology, data curation, visualization, writing. M.M.: data curation, investigation. X.W.: conceptualization, writing—review & editing, supervision, project administration, funding acquisition. Y.W.: investigation. F.Z.: investigation. M.W.: investigation. Q.X.: investigation. Z.L.: supervision. Y.S.: supervision. Complete contact information is available at: https://pubs.acs.org/

Notes

The authors declare no competing financial interest.

■ ACKNOWLEDGMENTS

This work was supported by funds from the National Natural Science Foundation of China (21905242, 21905205, 22065033, 21965034, and U1903217) and the Natural Science Foundation of Xinjiang Province (2022D01E35, 2022D01A105, and 2022B01024).

■ REFERENCES

(1) Chuai, M.; Yang, J.; Wang, M.; Yuan, Y.; Liu, Z.; Xu, Y.; Yin, Y.; Sun, J.; Zheng, X.; Chen, N.; Chen, W. High-performance Zn battery with transition metal ions co-regulated electrolytic MnO_2. *eScience* **2021**, *1*, 178−185.

(2) Song, M.; Tan, H.; Chao, D.; Fan, H. J. Recent advances in Zn-ion batteries. *Adv. Funct. Mater.* **2018**, *28*, No. 1802564.

(3) Pang, Q.; Sun, C.; Yu, Y.; Zhao, K.; Zhang, Z.; Voyles, P. M.; Chen, G.; Wei, Y.; Wang, X. $H_2V_3O_8$ nanowire/graphene electrodes for aqueous rechargeable zinc ion batteries with high rate capability and large capacity. *Adv. Energy Mater.* **2018**, *8*, No. 1800144.

(4) Li, H.; Ma, L.; Han, C.; Wang, Z.; Liu, Z.; Tang, Z.; Zhi, C. Advanced rechargeable zinc-based batteries: recent progress and future perspectives. *Nano Energy* **2019**, *62*, 550−587.

(5) Naveed, A.; Rasheed, T.; Raza, B.; Chen, J.; Yang, J.; Yanna, N.; Wang, J. Addressing thermodynamic Instability of Zn anode: classical and recent advancements. *Energy Storage Mater.* **2022**, *44*, 206−230.

(6) Bayaguud, A.; Fu, Y.; Zhu, C. Interfacial parasitic reactions of zinc anodes in zinc ion batteries: Underestimated corrosion and hydrogen evolution reactions and their suppression strategies. *J. Energy Chem.* **2022**, *64*, 246−262.

(7) Cui, J.; Liu, X.; Xie, Y.; Wu, K.; Wang, Y.; Liu, Y.; Zhang, J.; Yi, J.; Xia, Y. Improved electrochemical reversibility of Zn plating/stripping: A promising approach to suppress water-induced issues through the formation of H-bonding. *Mater. Today Energy* **2020**, *18*, No. 100563.

(8) Jin, Y.; Han, K. S.; Shao, Y.; Sushko, M. L.; Xiao, J.; Pan, H.; Liu, J. Stabilizing zinc anode reactions by polyethylene oxide polymer in mild aqueous electrolytes. *Adv. Funct. Mater.* **2020**, *30*, No. 2003932.

(9) Zeng, X.; Liu, J.; Mao, J.; Hao, J.; Wang, Z.; Zhou, S.; Ling, C. D.; Guo, Z. Toward a reversible Mn^{4+}/Mn^{2+} redox reaction and dendrite-free Zn anode in near-neutral aqueous Zn/MnO_2 batteries via salt anion chemistry. *Adv. Energy Mater.* **2020**, *10*, No. 1904163.

(10) Zhao, K.; Liu, F.; Fan, G.; Liu, J.; Yu, M.; Yan, Z.; Zhang, N.; Cheng, F. Stabilizing zinc electrodes with a vanillin additive in mild aqueous electrolytes. *ACS Appl. Mater. Interfaces* **2021**, *13*, 47650−47658.

(11) Shi, J.; Xia, K.; Liu, L.; Liu, C.; Zhang, Q.; Li, L.; Zhou, X.; Liang, J.; Tao, Z. Ultrahigh coulombic efficiency and long-life aqueous Zn anodes enabled by electrolyte additive of acetonitrile. *Electrochim. Acta* **2020**, *358*, No. 136937.

(12) Wang, Z.; Zhou, M.; Qin, L.; Chen, M.; Chen, Z.; Guo, S.; Wang, L.; Fang, G.; Liang, S. Simultaneous regulation of cations and anions in an electrolyte for high-capacity, high-stability aqueous zinc−vanadium batteries. *eScience* **2022**, *2*, 209−218.

(13) Wu, K.; Ning, F.; Yi, J.; Liu, X.; Qin, J.; Liu, Y.; Zhang, J. Host-guest supramolecular interaction behavior at the interface between anode and electrolyte for long life Zn anode. *J. Energy Chem.* **2022**, *69*, 237−243.

(14) Ji, X. A perspective of ZnCl2 electrolytes: The physical and electrochemical properties. *eScience* **2021**, *1*, 99−107.

(15) Ni, Q.; Jiang, H.; Sandstrom, S.; Bai, Y.; Ren, H.; Wu, X.; Guo, Q.; Yu, D.; Wu, C.; Ji, X. A $Na_3V_2(PO_4)_2O_{1.6}F_{1.4}$ cathode of Zn-ion battery enabled by a water-in-bisalt electrolyte. *Adv. Funct. Mater.* **2020**, *30*, No. 2003511.

(16) Chen, S.; Lan, R.; Humphreys, J.; Tao, S. Salt-concentrated acetate electrolytes for a high voltage aqueous Zn/MnO_2 battery. *Energy Storage Mater.* **2020**, *28*, 205−215.

(17) Zhang, C.; Holoubek, J.; Wu, X.; Daniyar, A.; Zhu, L.; Chen, C.; Leonard, D. P.; Rodriguez-Perez, I. A.; Jiang, J. X.; Fang, C.; Ji, X.

A $ZnCl_2$ water-in-salt electrolyte for a reversible Zn metal anode. *Chem. Commun.* **2018**, *54*, 14097−14099.
(18) Liu, J.; Long, J.; Shen, Z.; Jin, X.; Han, T.; Si, T.; Zhang, H. A self-healing flexible quasi-solid zinc-Ion battery using all-in-one electrodes. *Adv. Sci.* **2021**, *8*, No. 2004689.
(19) Wang, Z.; Hu, J.; Han, L.; Wang, Z.; Wang, H.; Zhao, Q.; Liu, J.; Pan, F. A MOF-based single-ion Zn^{2+} solid electrolyte leading to dendrite-free rechargeable Zn batteries. *Nano Energy* **2019**, *56*, 92−99.
(20) Wang, Z.; Huang, J.; Guo, Z.; Dong, X.; Liu, Y.; Wang, Y.; Xia, Y. A metal-organic framework host for highly reversible dendrite-free zinc metal anodes. *Joule* **2019**, *3*, 1289−1300.
(21) Wu, K.; Cui, J.; Yi, J.; Liu, X.; Ning, F.; Liu, Y.; Zhang, J. Biodegradable Gel Electrolyte Suppressing Water-Induced Issues for Long-Life Zinc Metal Anodes. *ACS Appl. Mater. Interfaces* **2022**, *14*, 34612−34619.
(22) Zhao, Z.; Zhao, J.; Hu, Z.; Li, J.; Li, J.; Zhang, Y.; Wang, C.; Cui, G. Long-life and deeply rechargeable aqueous Zn anodes enabled by a multifunctional brightener-inspired interphase. *Energy Environ. Sci.* **2019**, *12*, 1938−1949.
(23) Hieu, L. T.; So, S.; Kim, I. T.; Hur, J. Zn anode with flexible β-PVDF coating for aqueous Zn-ion batteries with long cycle life. *Chem. Eng. J.* **2021**, *411*, No. 128584.
(24) Zhou, S.; Wang, Y.; Lu, H.; Zhang, Y.; Fu, C.; Usman, I.; Liu, Z.; Feng, M.; Fang, G.; Cao, X.; Liang, S.; Pan, A. Anti-corrosive and Zn-ion-regulating composite interlayer enabling long-life Zn metal anodes. *Adv. Funct. Mater.* **2021**, *31*, No. 2104361.
(25) Zhang, Y.; Cao, Z.; Liu, S.; Du, Z.; Cui, Y.; Gu, J.; Shi, Y.; Li, B.; Yang, S. Charge-enriched strategy based on MXene-based polypyrrole layers toward dendrite-free zinc metal anodes. *Adv. Energy Mater.* **2022**, *12*, No. 2103979.
(26) Li, Z.; Wu, L.; Dong, S.; Xu, T.; Li, S.; An, Y.; Jiang, J.; Zhang, X. Pencil drawing stable interface for reversible and durable aqueous zinc-ion batteries. *Adv. Funct. Mater.* **2020**, *31*, No. 2006495.
(27) Cao, Q.; Gao, H.; Gao, Y.; Yang, J.; Li, C.; Pu, J.; Du, J.; Yang, J.; Cai, D.; Pan, Z.; Guan, C.; Huang, W. Regulating dendrite-free zinc deposition by 3D zincopilic nitrogen-doped vertical graphene for high-performance flexible Zn-ion batteries. *Adv. Funct. Mater.* **2021**, *31*, No. 2103922.
(28) He, H.; Tong, H.; Song, X.; Song, X.; Liu, J. Highly stable Zn metal anodes enabled by atomic layer deposited Al_2O_3 coating for aqueous zinc-ion batteries. *J. Mater. Chem. A* **2020**, *8*, 7836−7846.
(29) Zhao, R.; Yang, Y.; Liu, G.; Zhu, R.; Huang, J.; Chen, Z.; Gao, Z.; Chen, X.; Qie, L. Redirected Zn electrodeposition by an anti-corrosion elastic constraint for highly reversible Zn anodes. *Adv. Funct. Mater.* **2020**, *31*, No. 2001867.
(30) Liu, H.; Wang, J. G.; Hua, W.; Sun, H.; Huyan, Y.; Tian, S.; Hou, Z.; Yang, J.; Wei, C.; Kang, F. Building ohmic contact interfaces toward ultrastable Zn metal anodes. *Adv. Sci.* **2021**, *8*, No. 2102612.
(31) Liang, P.; Yi, J.; Liu, X.; Wu, K.; Wang, Z.; Cui, J.; Liu, Y.; Wang, Y.; Xia, Y.; Zhang, J. Highly reversible Zn anode enabled by controllable formation of nucleation sites for Zn-based batteries. *Adv. Funct. Mater.* **2020**, *30*, No. 1908528.
(32) Wu, K.; Yi, J.; Liu, X.; Sun, Y.; Cui, J.; Xie, Y.; Liu, Y.; Xia, Y.; Zhang, J. Regulating Zn Deposition via an Artificial Solid−Electrolyte Interface with Aligned Dipoles for Long Life Zn Anode. *Nano-Micro Lett.* **2021**, *13*, No. 79.
(33) Yu, H.; Li, Q.; Liu, W.; Wang, H.; Ni, X.; Zhao, Q.; Wei, W.; Ji, X.; Chen, Y.; Chen, L. Fast ion diffusion alloy layer facilitating 3D mesh substrate for dendrite-free zinc-ion hybrid capacitors. *J. Energy Chem.* **2022**, *73*, 565−574.
(34) Zhang, N.; Huang, S.; Yuan, Z.; Zhu, J.; Zhao, Z.; Niu, Z. Direct self-assembly of MXene on Zn anodes for dendrite-free aqueous zinc-ion batteries. *Angew. Chem.* **2021**, *133*, 2897−2901.
(35) Li, X.; Li, M.; Luo, K.; Hou, Y.; Li, P.; Yang, Q.; Huang, Z.; Liang, G.; Chen, Z.; Du, S.; Huang, Q.; Zhi, C. Lattice matching and halogen regulation for synergistically induced uniform zinc electrodeposition by halogenated Ti_3C_2 MXenes. *ACS Nano* **2022**, *16*, 813−822.
(36) Tian, Y.; An, Y.; Yang, Y.; Xu, B. Robust nitrogen/selenium engineered MXene/ZnSe hierarchical multifunctional interfaces for dendrite-free zinc-metal batteries. *Energy Storage Mater.* **2022**, *49*, 122−134.
(37) Kim, G. H.; Shao, L.; Zhang, K.; Pipe, K. P. Engineered doping of organic semiconductors for enhanced thermoelectric efficiency. *Nat. Mater.* **2013**, *12*, 719−723.
(38) Cao, Z.; Zhu, X.; Xu, D.; Dong, P.; Chee, M. O. L.; Li, X.; Zhu, K.; Ye, M.; Shen, J. Eliminating Zn dendrites by commercial cyanoacrylate adhesive for zinc ion battery. *Energy Storage Mater.* **2021**, *36*, 132−138.

https://doi.org/10.1021/acs.iecr.2c03462
Ind. Eng. Chem. Res. 2023, 62, 1350−1357